Chinese Journal of Natural Medicines

Sanguinarine triggers apoptosis and ferroptosis synchronously by directly binding BiP in lung squamous cell carcinoma

Weidan Tan, Xinyu Wei, Changsheng Li, Huilan Wei, Fei Yu, Xiaoju Shen, Xiaoxiang Mo, Meifen Wei, Shangping Xing, Zhuo Luo, Jie Yang

Citation: Weidan Tan, Xinyu Wei, Changsheng Li, Huilan Wei, Fei Yu, Xiaoju Shen, Xiaoxiang Mo, Meifen Wei, Shangping Xing, Zhuo Luo, Jie Yang, Sanguinarine triggers apoptosis and ferroptosis synchronously by directly binding BiP in lung squamous cell carcinoma, Chinese Journal of Natural Medicines, 2026, 24(4), 427−439. doi: 10.1016/S1875−5364(26)61115−6.

View online: https://doi.org/10.1016/S1875−5364(26)61115−6

Chinese Journal of Natural Medicines 24 (2026) 427-439

Contents lists available at ScienceDirect

Chinese Journal of Natural Medicines

journal homepage: www.cjnmcpu.com/

Original article

Sanguinarine triggers apoptosis and ferroptosis synchronously by directly binding BiP in lung squamous cell carcinoma

Weidan Tan[a, b,Δ], Xinyu Wei[a,Δ], Changsheng Li[a,Δ], Huilan Wei[a], Fei Yu[c], Xiaoju Shen[d], Xiaoxiang Mo[b], Meifen Wei[a], Shangping Xing[a,*], Zhuo Luo[a,*], Jie Yang[a,*]

[a] *Department of Pharmacology, School of Pharmacy, Guangxi Medical University, Nanning 530021, China*
[b] *Department of Pharmacology, Maternal and Child Health Hospital of Guangxi Zhuang Autonomous Region, Nanning 530021, China*
[c] *Phase Ⅰ Clinical Trial Center, Zhejiang Hospital, Hangzhou 31000, China*
[d] *Department of Pharmacy, The First Affiliated Hospital of Guangxi Medical University, Nanning 530021, China*

ARTICLE INFO

Article history:
Received 22 March 2025
Revised 19 June 2025
Accepted 23 June 2025
Available online 20 April 2026

Keywords:
Lung squamous cell carcinoma
Sanguinarine
Apoptosis
Ferroptosis
BiP

ABSTRACT

Lung squamous cell carcinoma (LUSC) is a prevalent and aggressive form of lung cancer with limited therapeutic options. Sanguinarine (SAG), a prominent benzophenanthridine alkaloid derived from *Zanthoxylum nitidum* (Roxb.) DC, exhibits established anti-tumor activity; however, its molecular mechanisms in LUSC remain incompletely defined. In this study, the anti-cancer effects and underlying mechanisms of SAG were systematically investigated *in vitro* and *in vivo*. Cell viability and death were evaluated using methyl thiazolyl tetrazolium (MTT) assays, colony formation assays, flow cytometry, transmission electron microscopy (TEM), and Western blotting (WB). Drug affinity responsive target stability (DARTS) combined with liquid chromatography–tandem mass spectrometry (LC-MS/MS), molecular docking, cellular thermal shift assay (CETSA), and surface plasmon resonance (SPR) were employed to identify and validate molecular targets of SAG. The results demonstrated that SAG simultaneously induces apoptosis and ferroptosis in LUSC cells by directly targeting the endoplasmic reticulum (ER) chaperone binding immunoglobulin protein (BiP). Silencing of BiP markedly attenuated SAG-induced apoptosis and ferroptosis, confirming its essential role in this process. Mechanistically, SAG up-regulates BiP expression and activates the protein kinase R-like endoplasmic reticulum kinase (PERK)/eIF2α/C/EBP homologous protein (CHOP)/GADD34 signaling axis of ER stress (ERS), ultimately leading to dual induction of apoptosis and ferroptosis *in vitro* and *in vivo*.

1. Introduction

Lung squamous cell carcinoma (LUSC) accounts for 30%-40% of lung cancer cases and is characterized by high relapse rates, poor prognosis, and limited therapeutic options [1]. The development of targeted therapies for LUSC remains challenging due to substantial tumor heterogeneity, a relative scarcity of identifiable oncogenic driver mutations, and incomplete understanding of the underlying molecular mechanisms [2, 3]. Although advances in immunotherapy have improved clinical outcomes, a substantial proportion of patients experience immune-related adverse events (irAEs), which limit therapeutic efficacy and may contribute to disease progression [4]. Currently, platinum-based combination chemotherapy, typically involving cisplatin (DDP) or carboplatin paired with docetaxel, gemcitabine, or paclitaxel, remains the standard first-line treatment. However, these regimens are frequently associated with either intrinsic or acquired drug resistance, as well as significant nephrotoxicity, neurotoxicity, and ototoxicity [5]. Consequently, there is an urgent need to identify novel therapeutic agents that can improve clinical outcomes for LUSC patients.

Endoplasmic reticulum stress (ERS) plays a critical role in regulated cell death (RCD), including apoptosis [6], ferroptosis [7], autophagy [8], and pyroptosis [9]. ERS is triggered by cellular stressors such as hypoxia, nutrient deprivation, and protein misfolding, leading to activation of the unfolded protein response (UPR) to restore cellular homeostasis [10]. The UPR is mediated by the ER chaperone binding immunoglobulin protein (BiP) and three ER membrane-anchored stress sensors: protein kinase R-like endoplasmic reticulum kinase (PERK), inositol-requiring enzyme 1 (IRE1), and activating transcription factor 6 (ATF6), all of which bind to BiP under non-stressed conditions [11]. Upon ERS induction, BiP dissociates from these sensors, leading to their activation and initiation of the UPR. Elevated BiP expression has been associated with poor prognosis [12] and resistance to bortezomib in multiple cancers [13]. For example, the hydroxyquinoline analogue YUM70 directly targets BiP, inducing ERS-mediated apoptosis and enhancing cytotoxicity when combined with topotecan or vorinostat [14]. When ERS is excessive or sustained, the UPR from adaptive to pro-death signaling, ultimately triggering apoptosis or ferroptosis [15, 16]. Recent studies indicate that icetexane diterpenes enhance the BiP-ATF4-C/EBP homologous protein (CHOP) axis and strengthen BiP-ATF4 interactions, thereby promoting

* Corresponding author.
E-mail addresses: shopingxing@sr.gxmu.edu.cn (S. Xing); luozhuo@gxmu.edu.cn (Z. Luo); jieyang2016@gxmu.edu.cn (J. Yang)
Δ These authors contributed equally to this work.

https://doi.org/10.1016/S1875-5364(26)61115-6

ERS and apoptosis in colorectal cancer cells [17]. Similarly, ginsenoside compound K up-regulates BiP expression, suppresses phosphorylated (p)-signal transducer and activator of transcription 3 (STAT3) levels, and triggers ERS-dependent apoptosis in human liver cancer cells, highlighting BiP as a promising therapeutic target [18]. However, the mechanisms by which BiP mediates the crosstalk between apoptosis and ferroptosis in the context of ERS remain largely uncharacterized.

As a traditional Chinese medicinal material, *Zanthoxylum nitidum* (Roxb.) DC is commonly used in clinical practice to treat cough, pneumonia, asthma, and other respiratory conditions owing to its analgesic, anti-tussive, anti-bacterial, diuretic, and anti-inflammatory properties [19]. Sanguinarine (SAG) is a natural quaternary benzophenanthridine alkaloid isolated from *Zanthoxylum nitidum* (Roxb.) DC. Accumulating evidence demonstrates that SAG exhibits potent anti-tumor activity. For instance, SAG suppresses gastric tumor growth by modulating the TOX/DNA-PKcs/KU70/80 pathway [20], inhibits melanoma invasion and migration *via* the FAK/PI3K/AKT/mTOR signaling axis [21], and blocks proliferation and metastasis in non-small cell lung cancer (NSCLC) by regulating STUB1/glutathione peroxidase 4 (GPX4)-mediated ferroptosis [22]. Despite these findings, the precise molecular targets and mechanisms underlying SAG-mediated anti-tumor effects in LUSC remain unclear.

In the present study, we investigated the anti-tumor efficacy, molecular targets, and underlying mechanisms of SAG in LUSC using both *in vitro* and *in vivo* models. We demonstrate that SAG potently induces both apoptosis and ferroptosis in LUSC cells and xenograft models. Mechanistically, SAG directly binds to BiP, up-regulates its expression, and activates the PERK/eIF2α/CHOP/GADD34 signaling pathway of ERS. These findings provide new mechanistic insights into SAG-mediated anti-tumor activity and support the development of BiP-targeted therapeutic strategies for LUSC.

2. Materials and methods

2.1. Reagents and antibodies

SAG (Fig. 1A) (≥ 98% purity) was purchased from Solarbio (Beijing, China). DDP was obtained from Qilu Pharmaceutical Co., Ltd. (Jinan, China). Z-VAD-FMK (Z-VAD), ferrostatin-1 (Fer-1), liproxstatin-1 (Lipro-1), deferoxamine (DFO), disulfiram (DSF), necrosulfonamide (Nec), and chloroquine (CQ) were acquired from MedChemExpress (NJ, USA). Assay kits for Fe^{3+}, glutathione (GSH), malondialdehyde (MDA), and superoxide dismutase (SOD) were sourced from Solarbio (Beijing, China).

2.2. Cell culture and treatment

BEAS-2B cells (Cell Bank of the Chinese Academy of Sciences, Kunming, China) were maintained in LHC basal medium (Thermo Scientific, USA) supplemented with 1% penicillin-streptomycin solution (Solarbio, Beijing, China) and 10% fetal bovine serum (FBS) (Oricell Biotechnology, Guangzhou, China). SK-MES-1 and NCI-H226 cells (Cell Bank of the Chinese Academy of Sciences, Shanghai, China), along with NCI-H1703 and NCI-H2170 cells (National Collection of Authenticated Cell Cultures, Shanghai, China), were cultured in complete RPMI-1640 medium (Gibco, USA) containing 1% penicillin-streptomycin and 10% FBS. All cell were incubated at 37 °C in a humidified incubator with 5% CO_2.

2.3. Cell viability assay

Cell viability was assessed using the methyl thiazolyl tetrazolium (MTT) assay (Solarbio, Beijing, China). Cells were seeded in 96-well plates at a density of 1.5×10^4 cells/mL (200 μL per well).

Following SAG treatment, 20 μL of MTT reagent (5 mg·mL^{-1}) was added to each well and incubated for 4 h at 37 °C. The medium was then removed, and the resulting formazan crystals were dissolved in 200 μL of dimethyl sulfoxide (DMSO, Aladdin, Shanghai, China). Absorbance was measured at 490 nm using a microplate reader (BioTek, Vermont, USA). Data are presented as mean ± SD. The half maximal inhibitory concentration (IC_{50}) value was determined by non-linear regression analysis, and the selectivity index (SI) was calculated as follows: SI = [IC_{50} (normal cells) / IC_{50} (cancer cells)] × 100.

2.4. Colony formation assay

SK-MES-1 and H1703 cells were seeded in 6-well plates (400 cells per well) and treated with SAG or DDP for 14 days. Colonies were fixed with formalin, stained with 0.25% crystal violet, and counted when containing more than 50 cells. Colony formation efficiency was calculated as: (number of colonies formed / number of cells seeded) × 100%.

2.5. Cell cycle and apoptosis assays

SK-MES-1 and H1703 cells were seeded in 6-well plates at a density of 1×10^6 cells per well and exposed to SAG or DDP for 24 h. For cell cycle analysis, cells were fixed in ice-cold 70% ethanol overnight at 4 °C, stained with propidium iodide (PI) using the Cell Cycle Staining Kit (MultiSciences, Hangzhou, China), and analyzed by flow cytometry (BD, New Jersey, USA). For apoptosis detection, cells were harvested using EDTA-free trypsin, resuspended in 500 μL of 1 × binding buffer, and stained with Annexin V-APC/7-amino-actinomycin D (7-AAD) (MultiSciences, Hangzhou, China). Following a 15-minute incubation in the dark, apoptotic cells were quantified by flow cytometry.

2.6. Transmission electron microscopy (TEM)

SK-MES-1 and H1703 cells were seeded in 10 cm culture dishes and allowed to adhere. After SAG treatment, morphological features characteristic of apoptosis and ferroptosis were examined using a transmission electron microscope (Hitachi-7650, Japan).

2.7. Biochemical assays

Following 24 h of SAG treatment, SK-MES-1 and H1703 cells (seeded at 1×10^7 cells/well in 100 mm dishes) were harvested and lysed. Intracellular levels of target analytes were quantified using commercial kits according to the manufacturers' instructions: Fe^{3+} (Solarbio, #BC5315, 510 nm), Fe^{2+} (Solarbio, #BC5415, 593 nm), GSH (Jiancheng Bio, #A006-2-1, 405 nm), MDA (Solarbio, #BC0025, 532 nm), and SOD (Solarbio, #BC0175, 560 nm). All absorbance readings from the microplate reader were normalized to the negative control and expressed as percentages.

2.8. Western blotting (WB) assay

Cells were lysed in RIPA buffer (Solarbio, Beijing, China) containing PMSF (Solarbio, Beijing, China). Lysates were centrifuged at 12,000 × *g* for 30 min at 4 °C, and supernatants were collected. Protein concentrations were determined using a BCA assay kit (Beyotime Biotechnology, Shanghai, China). Equal amounts of protein were separated by sodium dodecyl sulfate-polyacrylamide gel electrophoresis (SDS-PAGE) and transferred onto nitrocellulose (NC) membranes (Millipore, Billerica, MA). Membranes

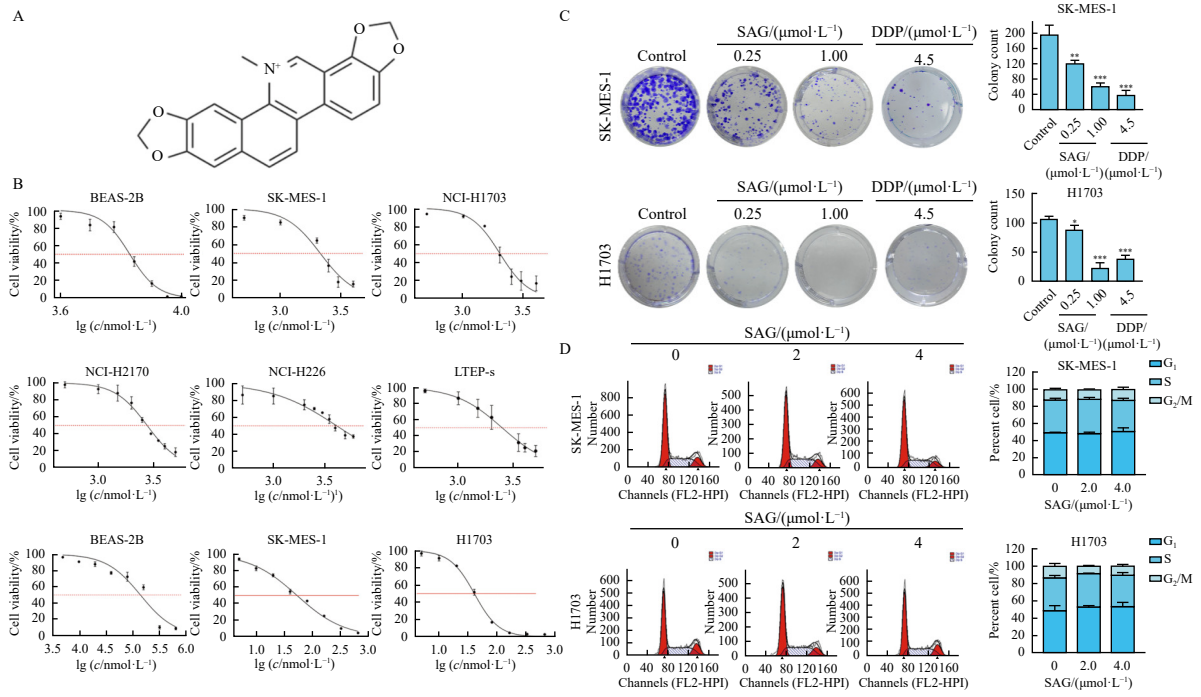

Fig. 1 SAG suppressed cell viability in LUSC cells. (A) Chemical structure of SAG. (B) BEAS-2B normal lung epithelial cells and eight LUSC cell lines were treated with different concentrations of SAG for 24 h, and cell viability was assessed by MTT assay. (C) Colony formation assays were performed in SK-MES-1 and H1703 cells treated with or without SAG or DDP for 10–14 d. (D) Cell cycle distribution of SK-MES-1 and H1703 cells with or without SAG treatment was analyzed by flow cytometry. Data are presented as mean ± SD (n = 3). $^{*}P < 0.05$, $^{**}P < 0.01$; n s., not significant ($P > 0.05$) compared with 0 μmol·L^{-1} SAG group.

were blocked with 5% non-fat milk for 1 h at room temperature and then incubated overnight at 4 °C with primary antibodies against GAPDH (Proteintech, Wuhan, China), PARP (Proteintech, Wuhan, China), Caspase 3 (Proteintech, Wuhan, China), cleaved Caspase 3 (ZEN-Bioscience, Chengdu, China), *β*-actin (ABclonal, Wuhan, China), B-cell lymphoma-2 (Bcl-2) (ZEN-Bioscience, Chengdu, China), Bcl-2-associated X protein (Bax) (Proteintech, Wuhan, China), nuclear factor erythroid 2-related factor 2 (NRF2) (ZEN-Bioscience, Chengdu, China), SLC7A11 (ZEN-Bioscience, Chengdu, China), heme oxygenase-1 (HO-1) (ZEN-Bioscience, Chengdu, China), GPX4 (Abcam, MA, USA), transferrin (TF) (ZEN-Bioscience, Chengdu, China), ferritin light chain (FLC) (ZEN-Bioscience, Chengdu, China), BiP (CST, Boston, USA), PERK (Proteintech, Wuhan, China), p-PERK (Proteintech, Wuhan, China), eIF2α (CST, Boston, USA), p-eIF2α (CST, Boston, USA), CHOP (Proteintech, Wuhan, China), GADD34 (ZEN-Bioscience, Chengdu, China), IRE1 (CST, Boston, USA), p-IRE1 (ABclonal, Wuhan, China), and ATF6 (ZEN-Bioscience, Chengdu, China). After three 5-minute washes with PBST, membranes were incubated with corresponding secondary antibodies (CST, Beverly, MA, USA) for 1 h at room temperature. Protein bands were visualized using an ECL WB detection reagent (4A Biotech, #4AW011, Beijing, China).

2.9. Cellular thermal shift assay (CETSA)

SK-MES-1 and H1703 cells cultured in 10 cm dishes were pretreated with SAG or an equal volume of DMSO for 2 h, detached with EDTA-trypsin, and resuspended in phosphate-buffered saline (PBS) containing 1% protease inhibitor cocktail. Cell suspensions were equally aliquoted into six 100 μL PCR tubes and heated at 37, 50, 53, 56, 59, and 62 °C for 3 min, followed by three freeze-thaw cycles in liquid nitrogen. After centrifugation (14,000 r·min^{-1}, 40 min, 4 °C), supernatants were collected and analyzed by WB.

2.10. Drug affinity responsive target stability (DARTS) assay

SK-MES-1 and H1703 cells were lysed in 500 μL of NP-40 lysis buffer supplemented with fresh protease and phosphatase inhibitors (Thermo Scientific, USA). The lysate was divided equally into two tubes and incubated with either SAG or DMSO on a shaker for 2 h at room temperature. Samples were then aliquoted into 100 μL PCR tubes and digested with varying concentrations of pronase E (MedChemExpress, USA) for 20 min at room temperature. Proteolysis was terminated by adding 5× loading buffer, and proteins were analyzed by WB.

2.11. Surface plasmon resonance (SPR) analysis

SPR measurements were performed using a BIAcore T200 instrument (Cytiva, Piscataway, NJ, USA). Purified BiP protein (50 μg·mL^{-1}, pH 4.0) was immobilized onto a Series S Sensor Chip CM5 (Cytiva, NJ, USA) *via* standard amine coupling. PBS containing 5% DMSO served as the running buffer. SAG was diluted in running buffer, and nine concentrations were injected simultaneously at a flow rate of 30 μL·min^{-1} for a 120-second association phase at 25 °C. Blank-subtracted sensorgrams were generated, and data were processed using BIAcore T200 evaluation software (Cytiva, NJ, USA) to fit an appropriate binding model and determine the equilibrium dissociation constant (K_d).

2.12. Plasmid construction and transfection

A small interfering ribonucleic acid (siRNA) specifically targeting BiP was designed (RiboBio, Guangzhou, China). SK-MES-1 and H1703 cells were transfected with either si-NC or si-BiP using Lipo3000 (Thermo Scientific, USA) according to the manufacturer's instructions. At 24 h post-transfection, the medium was replaced with complete culture medium, and cells were subsequently treated with SAG.

2.13. Bioinformatic analysis

The Kyoto Encyclopedia of Genes and Genomes (KEGG) database was used for functional enrichment analysis. Gene sets were considered significantly enriched when the minimum size was 5, the maximum size was 5000, and both $P < 0.05$ and false discov-

ery rate (FDR) < 0.25. Molecular docking between SAG and BiP was performed using AutoDock software to calculate binding free energy, and interaction results were further analyzed and visualized using PyMOL.

2.14. Animal experiments

Animal experiments were conducted in accordance with a protocol approved by the Ethics Committee of Guangxi Medical University (approval number: No. 202206013). Briefly, BALB/c nude mice were purchased and housed at the Guangxi Medical University Laboratory Animal Center. SK-MES-1 cells (approximately 2.5×10^6 cells in 0.1 mL of cold PBS per mouse) were subcutaneously injected into the the right axillary region of 4-week-old mice. When tumor volumes reached 50–80 mm^3, mice were randomly assigned to four groups (n = 5): normal saline, DDP (5 $mg \cdot kg^{-1} \cdot wk^{-1}$), low-dose SAG (5 $mg \cdot kg^{-1} \cdot wk^{-1}$), and high-dose SAG (8 $mg \cdot kg^{-1} \cdot wk^{-1}$). Body weight and tumor size were measured every two days. Tumor volume (mm^3) was calculated using the formula: (tumor length × tumor $width^2$)/2.

2.15. Haematoxylin and eosin (HE) staining

Tumor and tissue sections were deparaffinized, rehydrated, and stained with hematoxylin for 6 min, followed by eosin counterstaining for 12 min. After differentiation, sections were sealed with neutral resin, dried, and examined under a microscope (NIKON, Japan).

2.16. Statistical analysis

Statistical analyses were performed using SPSS 20.0 (IBM, US) and GraphPad Prism 8 software (La Jolla, US). Data are presented as mean ± SD. Comparisons between two groups were conducted using an unpaired Student's t-test, while multiple comparisons were analyzed by one-way ANOVA. A $P < 0.05$ was considered statistically significant ($^{*}P < 0.05$; $^{**}P < 0.01$; $^{***}P < 0.001$). All experiments were independently repeated at least three times, and consistent results were subjected to statistical comparison.

3. Results

3.1. SAG triggers cell death and inhibits the proliferation of LUSC cells

The anti-tumor effect of SAG was evaluated in five human LUSC cell lines (SK-MES-1, NCI-H1703, NCI-H2170, NCI-H226, and LTEP-s), and its toxicity was assessed in immortalized human normal lung epithelial cells (BEAS-2B) following 24-h treatment with varying SAG concentrations; DDP served as a positive control. As shown in Fig. 1B and Table 1, SAG exhibited stronger inhibition of cell viability and a higher selectivity index (SI) across LUSC cell lines compared with DDP. Among these, SK-MES-1 and H1703 cells displayed the highest SI values and were therefore selected for subsequent experiments. SAG significantly suppressed the clonogenic proliferation capacity of SK-MES-1 and H1703 cells (Fig. 1C) but did not markedly alter their cell cycle distribution (Fig. 1D). Collectively, these findings indicate that SAG inhibits LUSC cell proliferation primarily through induction of cell death rather than cell cycle arrest.

3.2. Apoptosis and ferroptosis synergistically contribute to SAG-induced death in LUSC cells

To determine the modes of cell death induced by SAG, several pharmacological inhibitors were employed. Pretreatment with Z-VAD (an apoptosis inhibitor) (Fig. 2A), Fer-1 (a ferroptosis inhibitor) (Fig. 2B), or Lipro-1 (another ferroptosis inhibitor) (Fig. 2C) significantly attenuated SAG-induced cell death. In contrast, pretreatment with DFO (an iron chelator) (Fig. 2D), DSF (a pyroptosis inhibitor) (Fig. 2E), CQ (an autophagy inhibitor) (Fig. 2F), or Nec (a necroptosis inhibitor) (Fig. 2G) failed to reduce SAG-induced cytotoxicity in LUSC cells. These results suggest that SAG induces cell death predominantly through apoptosis and ferroptosis.

TEM further confirmed these observations. SAG-treated cells exhibited typical apoptotic features, including cytoplasmic shrinkage, nuclear fragmentation, and apoptotic body formation, as well as endoplasmic reticulum (ER) swelling and vacuolization (Fig. 3A). Flow cytometric analysis using Annexin V-APC/7-AAD staining demonstrated a marked increase in apoptosis following SAG treatment, which was partially reversed by Z-VAD (Fig. 3B). WB showed that SAG significantly increased levels of cleaved PARP, cleaved Caspase 3, and Bax while suppressing Bcl-2 expression (Figs. 3C–3D). Mitochondrial abnormalities, including shrinkage, reduced volume, increased membrane density, and cristae loss or disappearance were observed (Fig. 3E). Concurrently, SAG markedly elevated intracellular Fe^{3+}, Fe^{2+}, and MDA levels while significantly reducing GSH content and SOD activity (Fig. 3F). Moreover, SAG decreased protein levels of NRF2, GPX4, and FLC, all negative regulators of ferroptosis, while increasing HO-1 and TF levels, with no significant effect on SLC7A11 (Figs. 3G–3H). These data collectively demonstrate that SAG concurrently induces apoptosis and ferroptosis in LUSC cells.

3.3. SAG directly binds to BiP in LUSC cells

To elucidate the mechanism underlying SAG-induced apoptosis and ferroptosis, DARTS coupled with liquid chromatography-tandem mass spectrometry (LC-MS/MS) was used to identify potential SAG-binding proteins. As outlined in Fig. 4A, SAG-treated and control lysates were subjected to pronase E digestion, followed by SDS-PAGE and Coomassie staining. Distinct protein bands within the 70-100 kDa range (highlighted by the red box) were observed in SAG-treated samples (Fig. 4B). Among the top 10 significantly enriched proteins, BiP, a member of the Hsp70 family and a prognostic marker in multiple cancers [23], was identified as the top candidate. KEGG pathway analysis revealed that

Table 1 IC_{50} and SI of SAG on human bronchial epithelial normal cells and LUSC cells for 24 h (Mean ± SD, n = 3).

Cell lines		IC_{50} ($\mu mol \cdot L^{-1}$) of SAG	SI value of SAG	IC_{50} ($\mu mol \cdot L^{-1}$) of DDP	SI value of DDP
Normal lung cell	BEAS-2B	6.480 ± 0.159	-	119.04 ± 4.67	-
LUSC	SK-MES-1	1.934 ± 0.081	3.35	51.66 ± 3.043	2.30
	NCI-H1703	1.978 ± 0.220	3.28	40.303 ± 3.39	2.95
	NCI-H2170	2.747 ± 0.161	2.36	-	-
	NCI-H226	4.449 ± 0.119	1.45	-	-
	LTEP-s	2.655 ± 0.564	2.44	-	-

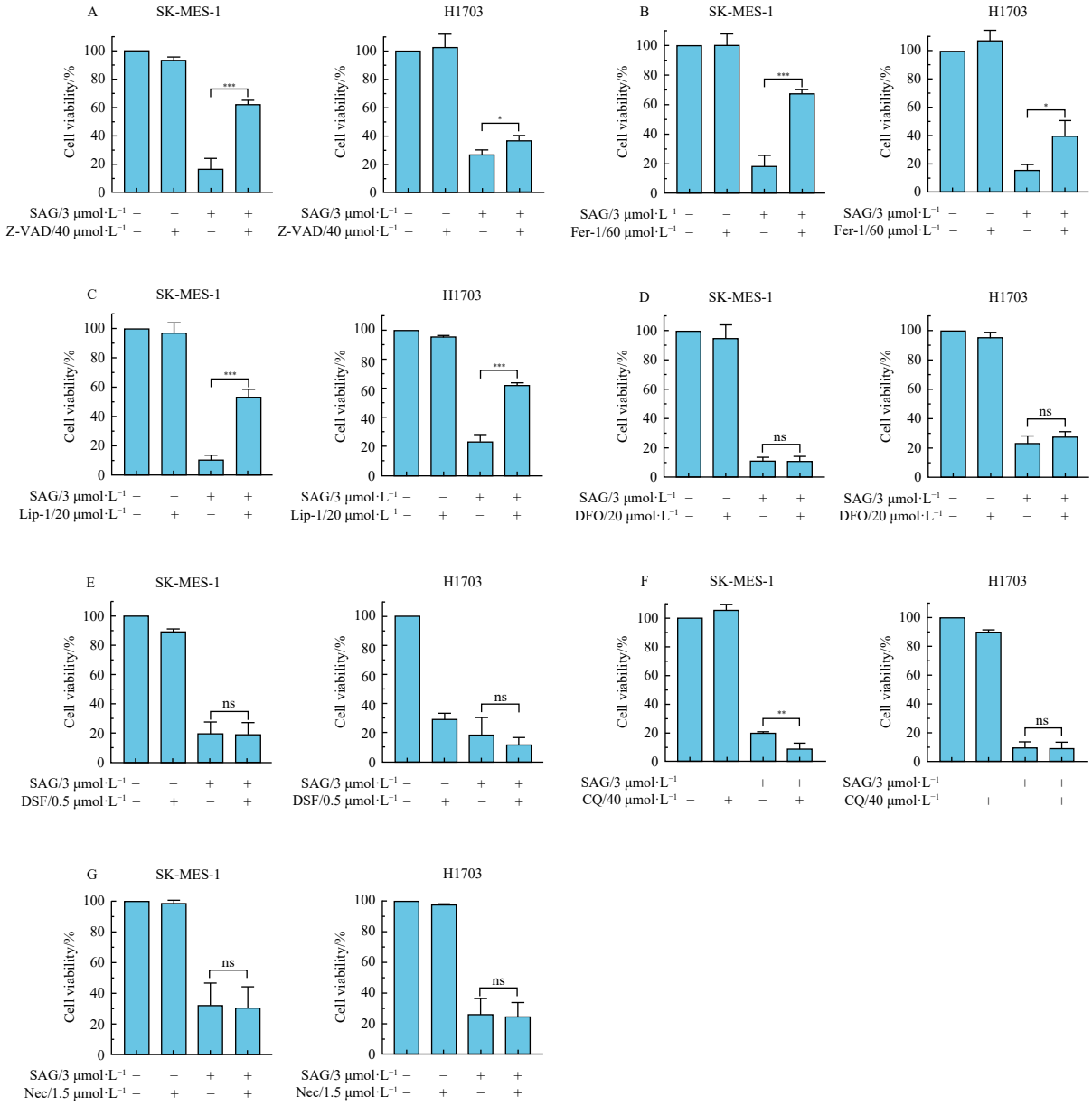

Fig. 2 SAG induces cell death on LUSC cells. SK-MES-1 and H1703 cells were treated with SAG and (A), Z-VAD-FMK, (B), Fer-1, (C), Lip-1, (D), DFO, (E), DSF, (F), CQ, (G), Nec respectively and detected by MTT assay. Data are expressed as mean ± SD (n = 3). $^{*}P < 0.05$, $^{**}P < 0.01$, $^{***}P < 0.001$; n s., not significant ($P > 0.05$) compared with 0 μmol·L^{-1} SAG group.

"protein processing in the endoplasmic reticulum" was the most significantly enriched pathway among the top 10 (Fig. 4C). Based on these findings, DARTS, CETSA, and SPR were performed to validate BiP as a direct SAG target. SAG markedly protected BiP from both pronase E-mediated proteolysis (Figs. 4E) and thermal denaturation (4F), indicating direct binding. Molecular docking using AutoDock predicted hydrogen bonds between SAG (PubChem CID: 5154) and BiP residues ASN-59, LYS-296, and SER-365 (UniProtKB/Swiss-Prot: P59769), with a binding energy of −9.4 kJ·mol^{-1} (Fig. 4G). SPR SPR analysis further confirmed dose-dependent binding, with a dissociation constant K_d of 64.07 μmol·L^{-1} (Fig. 4H). Thus, BiP is a direct molecular target of SAG in LUSC cells.

3.4. SAG promotes apoptosis and ferroptosis via BiP-mediated induction of ERS

Given BiP's central role in regulating ERS, its involvement in SAG-induced cell death was investigated. siRNA-mediated knockdown of BiP (Fig. 5A) significantly attenuated SAG-induced apoptosis and ferroptosis in both SK-MES-1 and H1703 cells (Fig. 5B). BiP depletion markedly reduced the SAG-induced increase in the Bax/Bcl-2 ratio (Fig. 5C) and reversed the SAG-mediated down-regulation of NRF2 and GPX4 (Fig. 5D), indicating that BiP is essential for SAG-induced cell death.

Next, we found that SAG up-regulated BiP protein expression in both dose- (2 and 4 μmol·L^{-1}) and time-dependent (6, 12, and 24 h) manners (Figs. 6A–6B). SAG also exacerbated ER expansion, swelling, and vacuolization compared to vehicle control (Fig. 6C). Since reactive oxygen species (ROS) generation is a key feature of ERS, intracellular ROS levels were assessed using the fluorescent probe DCFH-DA. SAG treatment significantly increased ROS accumulation in LUSC cells (Fig. 6D). Laser confocal microscopy revealed that SAG predominantly localized to the perinuclear ER in SK-MES-1 and H1703 cells (Fig. 6E). Among the three canonical ERS sensors, PERK, IRE1, and ATF6-SAG specifically increased p-PERK levels without affecting p-IRE1 or ATF6, indicating selective activation of the PERK pathway. SAG also up-regulated downstream effectors, including eIF2α, p-eIF2α, CHOP, and GADD34 (Fig. 6F). Importantly, BiP knockdown markedly at-

tenuated activation of the PERK/eIF2α/CHOP/GADD34 signaling axis (Fig. 6G). These findings indicate that SAG promotes apoptosis and ferroptosis via BiP-mediated activation of ER stress pathways.

3.5. SAG suppresses tumor growth via ERS-mediated apoptosis and ferroptosis in vivo

To determine whether SAG's *in vivo* anti-tumor effects, SK-MES-1 cells were subcutaneously implanted into the right flanks of nude mice. Seven days post-inoculation, mice received intraperitoneal injections of DDP (5 mg·kg^{-1}·wk^{-1}), low-dose SAG (5 mg·kg^{-1}·wk^{-1}), high-dose SAG (8 mg·kg^{-1}·wk^{-1}), or saline for 14 days (Fig. 7A). SAG significantly reduced tumor volume (Fig. 7B-7C) and weight (Fig. 7D), with efficacy comparable to DDP. Notably, body weight in the DDP group showed a declining trend, whereas SAG groups remained stable (Fig. 7E). HE staining showed that control tumors exhibited dense cellular architecture and active proliferation, whereas SAG- and DDP-treated tumors displayed reduced cell density, cytoplasmic leakage, vacuolization, and nuclear fragmentation (Fig. 7F). SAG treatment increased the Bax/Bcl-2 ratio and decreased NRF2 and GPX4 expression (Figs. 7G–7H), consistent with induction of apoptosis and ferroptosis. Furthermore, ERS markers, including p-PERK, BiP, GADD34, p-eIF2α, and CHOP, were significantly upregulated in SAG-treated tumors (Fig. 7I), confirming ERS activation. Collectively, SAG inhibits LUSC tumor growth *in vivo* by inducing ERS-mediated apoptosis and ferroptosis.

4. Discussion

LUSC is associated with high mortality and a paucity of targeted therapies, leaving patients with advanced disease with limited treatment options [2]. Given this urgent clinical need, novel LUSC-specific therapeutics are imperative. In this study, using *in vitro* and *in* xenograft models, we demonstrate that SAG exerts potent anti-LUSC activity by concurrently inducing apoptosis and ferroptosis. Mechanistically, SAG directly binds to and up-regulates the ER chaperone BiP, thereby activating the PERK/eIF2α/CHOP/GADD34 arm of the UPR and triggering cell death.

As a natural benzophenanthridine alkaloid, SAG exhibits diverse pharmacological activities, particularly anti-cancer effects. Prior studies report SAG's efficacy against various malignancies [24, 25] through apoptosis induction, cell cycle arrest, or inhibition of invasion [26]. Notably, SAG has been identified as a natural lysine-specific demethylase 1 (LSD1) inhibitor that suppresses

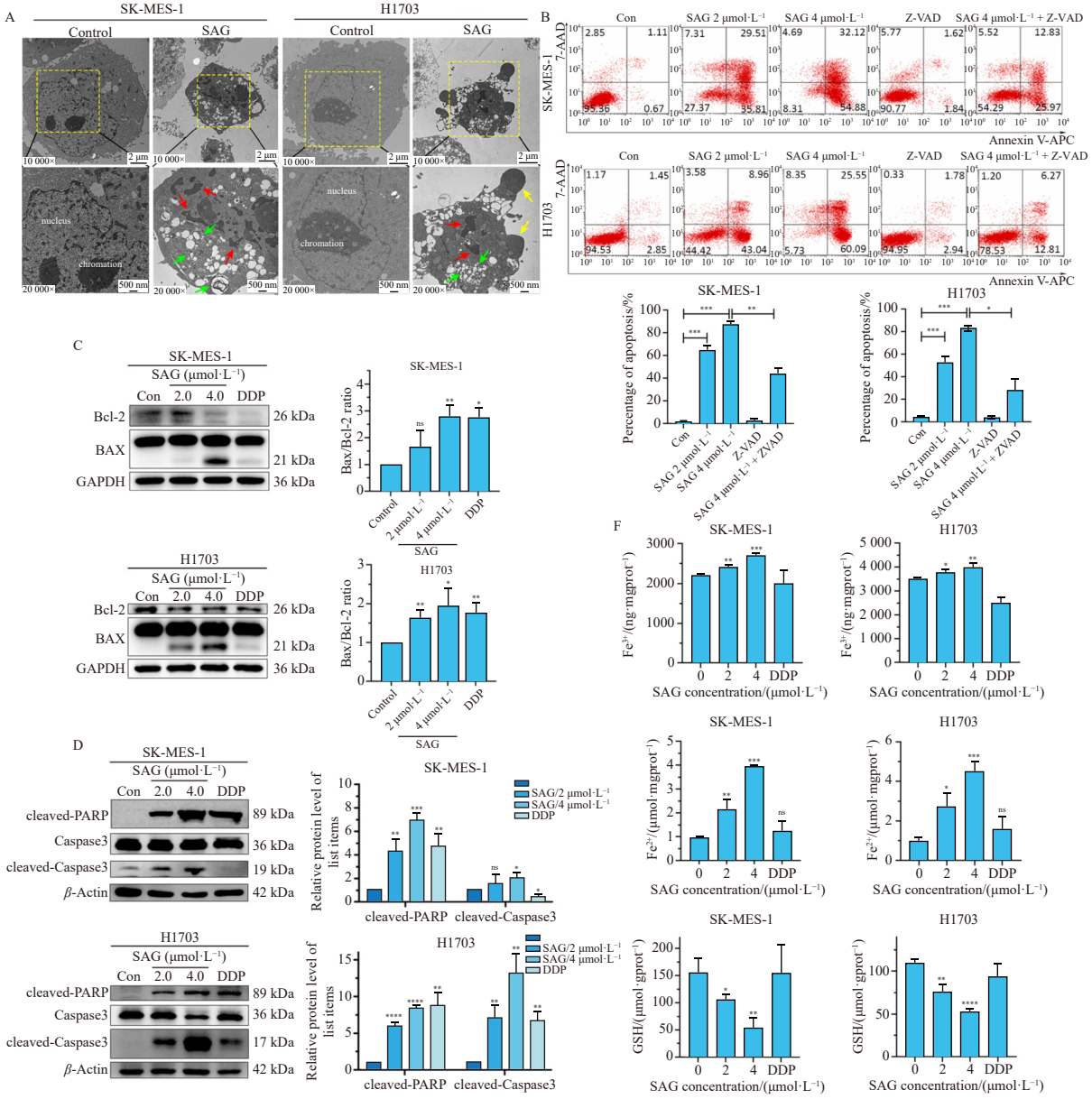

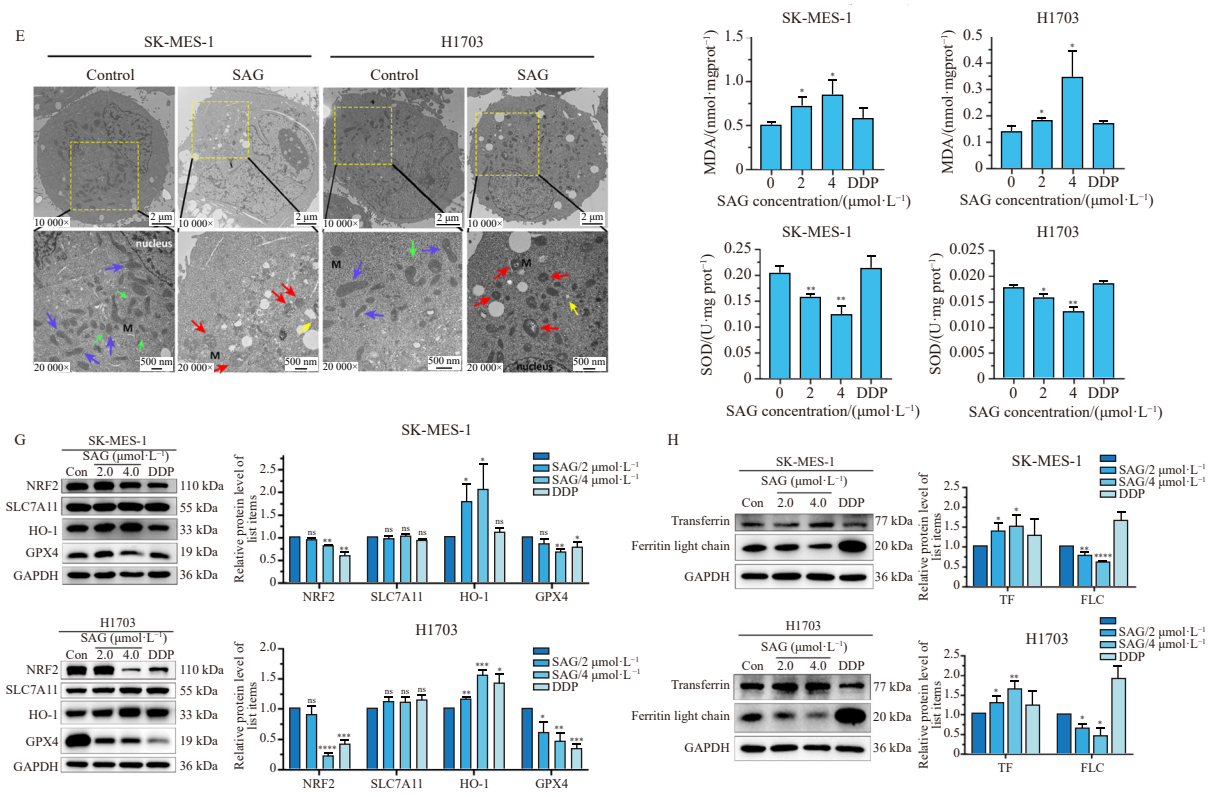

Fig. 3 SAG induces apoptosis and ferroptosis in LUSC cells. (A) SK-MES-1 and H1703 cells were treated with SAG or for 24 h and microscopic imaging was captured by transmission electron microscopy. Scale bar 2 μm and 500 nm. Red arrows indicate nuclear fragmentation, green arrows indicate damaged endoplasmic reticulum, and yellow arrows indicate apoptotic bodies. (B) The cell apoptosis rate of SK-MES-1 and H1703 cells with or without SAG treatment and with or without Z-VAD combination was detected by flow cytometry. (C–D) WB assay for investigating changes of the protein expression of Bcl-2, Bax, cleaved PARP, Caspase 3 and cleaved Caspase 3 of LUSC cells after treatment with SAG or DDP. (E) SK-MES-1 and H1703 cells were treated with SAG or for 24 h and microscopic imaging was captured by transmission electron microscopy. Scale bar 2 μm and 500 nm. Blue arrows indicate normal mitochondria, red arrows indicate damaged mitochondria, and yellow arrows indicate damaged endoplasmic reticulum. (F) The level of Fe^{3+}, Fe^{2+}, GSH, MDA, and SOD activity and were measured in the treated SK-MES-1 and H1703 cells. (G–H) WB assay for investigating changes of the protein expression of NRF2, SLC7A11, HO-1, GPX4, Transferrin and FLC of SK-MES-1, H1703 cells after treatment with SAG or DDP. Results are expressed as mean ± SD (n = 3). $^{*}P < 0.05$, $^{**}P < 0.01$, $^{***}P < 0.001$, and n s., not significant ($P > 0.05$) when compared to 0 μmol·L^{-1} SAG group.

lung adenocarcinoma (LUAD) growth and migration [27]. It also induces LUAD apoptosis *via* ROS generation and JAK/STAT pathway suppression [28], and promotes ferroptosis through modulation of the STUB1/GPX4 axis [22]. However, its role in LUSC has remained unclear. In this study, SAG exhibited stronger inhibition of cell viability and clonogenicity than DDP, along with a higher

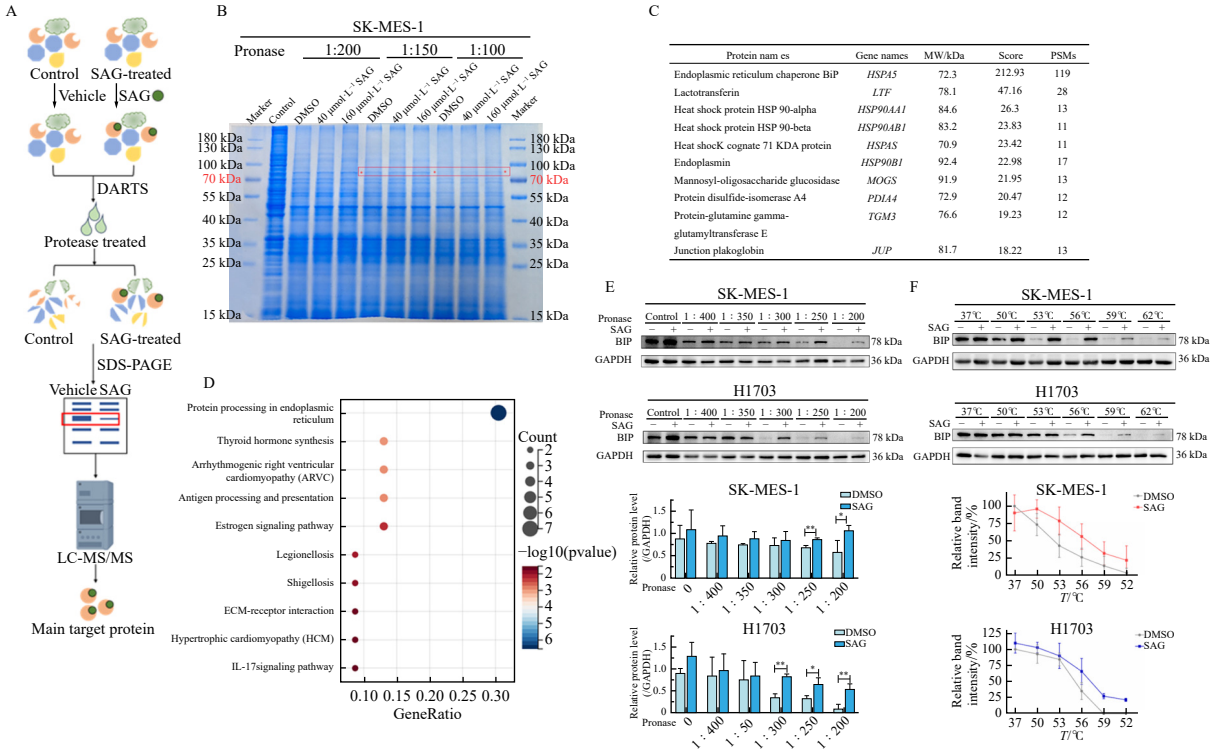

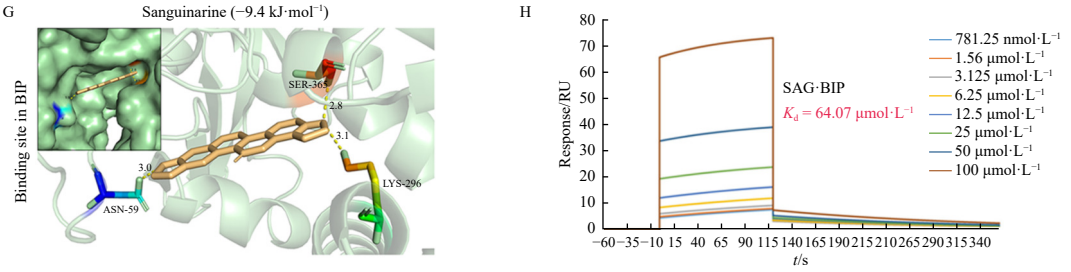

Fig. 4 Identification of SAG binding proteins. (A) Schematic representation showing procedures for identifying SAG-binding proteins by using DARTS and LC/LC-MS analyses. (B) SAG solution was co-incubated with the protein lysate of SK-MES-1. The bands were developed by SDS-PAGE after being treated with various concentrations' pronase. In the red frame is the protein band with improved stability against enzymatic hydrolysis. (C–D) KEGG analysis of the 43 SAG-binding proteins by DAVID. (E) DARTS method proved that SAG could improve the anti-enzymatic stability of BiP. (F) CETSA experiment verified that SAG can improve the thermal stability of BiP. (G) Autodock software simulates the 3D schematic diagram of SAG and BiP' interaction. (H) SPR assay verified the direct combination of SAG and BiP *in vitro*. Results are expressed as mean ± SD (n = 3). $^{*}P < 0.05$, $^{**}P < 0.01$, $^{***}P < 0.001$, and n s., not significant ($P > 0.05$) when compared to 0 μmol·L^{-1} SAG group.

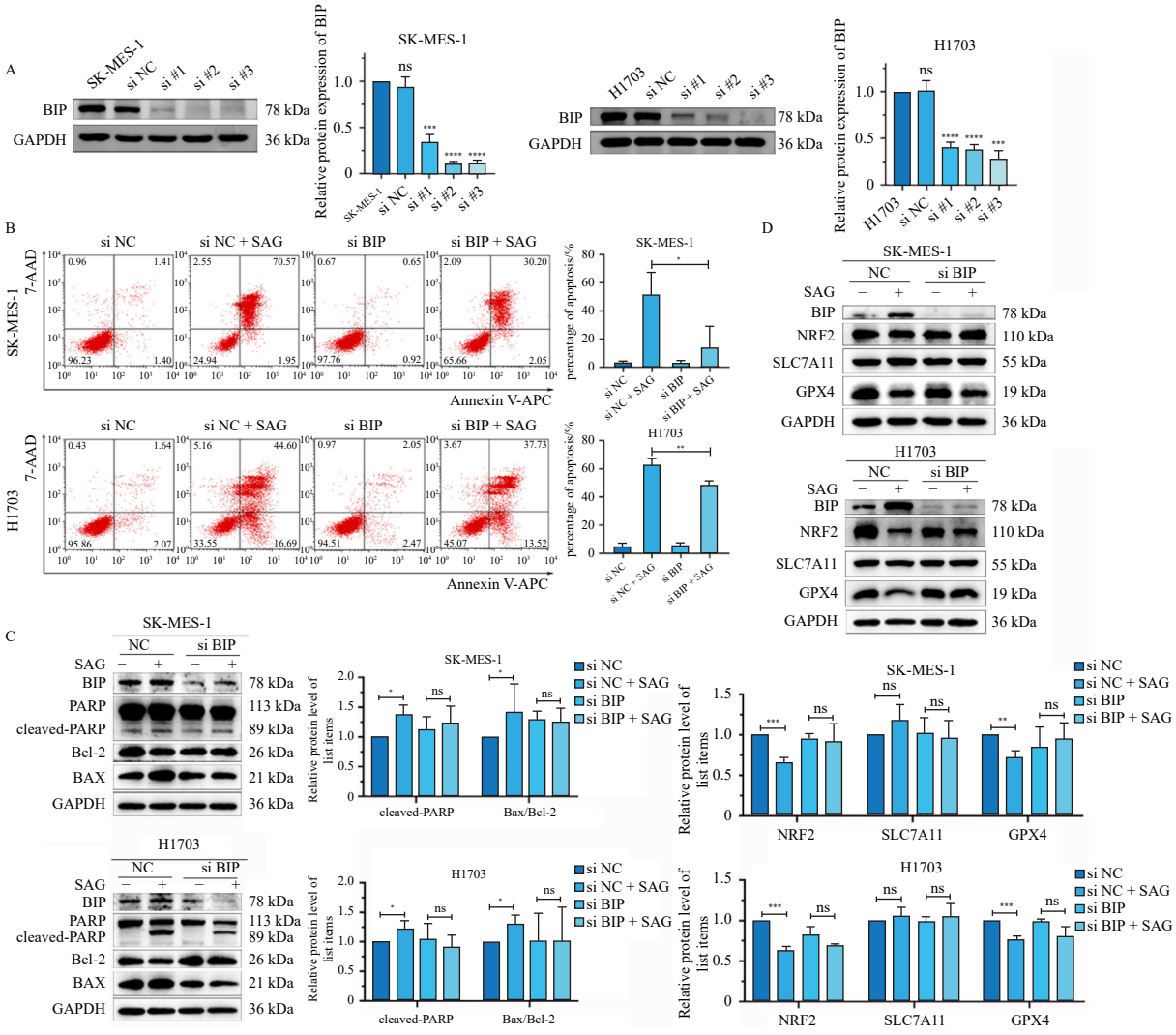

Fig. 5 SAG induces SK-MES-1 and H1703 cells apoptosis and ferroptosis by regulating BiP protein. (A) The expression of BiP protein in SK-MES-1 and H1703 cells after instantaneous transfection with siRNA. (B) The effect on the apoptosis of SK-MES-1 and H1703 cells after the interference BiP expression. (C) The expression of cleave-PARP, Bcl-2 and Bax of SK-MES-1 and H1703 cells after interference with BiP and treated by SAG. (D) The expression of NRF2, SLC7A11, GPX4 in SK-MES-1 and H1703 cells after interference with BiP and treated by SAG. Results are expressed as mean ± SD (n = 3). $^{*}P < 0.05$, $^{**}P < 0.01$, $^{***}P < 0.001$, and n s., not significant ($P > 0.05$) when compared to 0 μmol·L^{-1} SAG group.

selectivity index across five LUSC cell lines. Pharmacological inhibition assays demonstrated that SAG induces both apoptosis and ferroptosis. These findings were supported by TEM, flow cytometry, and WB analyses, which confirmed activation of apoptotic signaling (Caspase-3/PARP cleavage, increased Bax, and decreased Bcl-2) and ferroptotic alterations (iron accumulation, lipid peroxidation, GSH depletion, reduced SOD activity, downregulation of NRF2/GPX4/FLC, and upregulation of HO-1 and transferrin). Consistent results were observed *in vivo*, where SAG suppressed xenograft growth and induced apoptosis, ferroptosis, and ERS. These findings demonstrate that SAG exerts robust anti-LUSC effects through dual induction of apoptosis and ferroptosis, highlighting a previously uncharacterized therapeutic role. Notably, LUSC shares molecular and pathological features with other squamous cell carcinomas (SCCs), including those of the oesophagus, head and neck, anogenital region, and skin [2]. Therefore,

the therapeutic potential of SAG may extend beyond LUSC to other SCCs.

Resistance to cell death is a hallmark of cancer [29]. However, clinical translation of monotherapies targeting single RCD pathways is hindered by the extensive crosstalk among cell death pathways [30]. Increasing evidence indicates that apoptosis and fer-

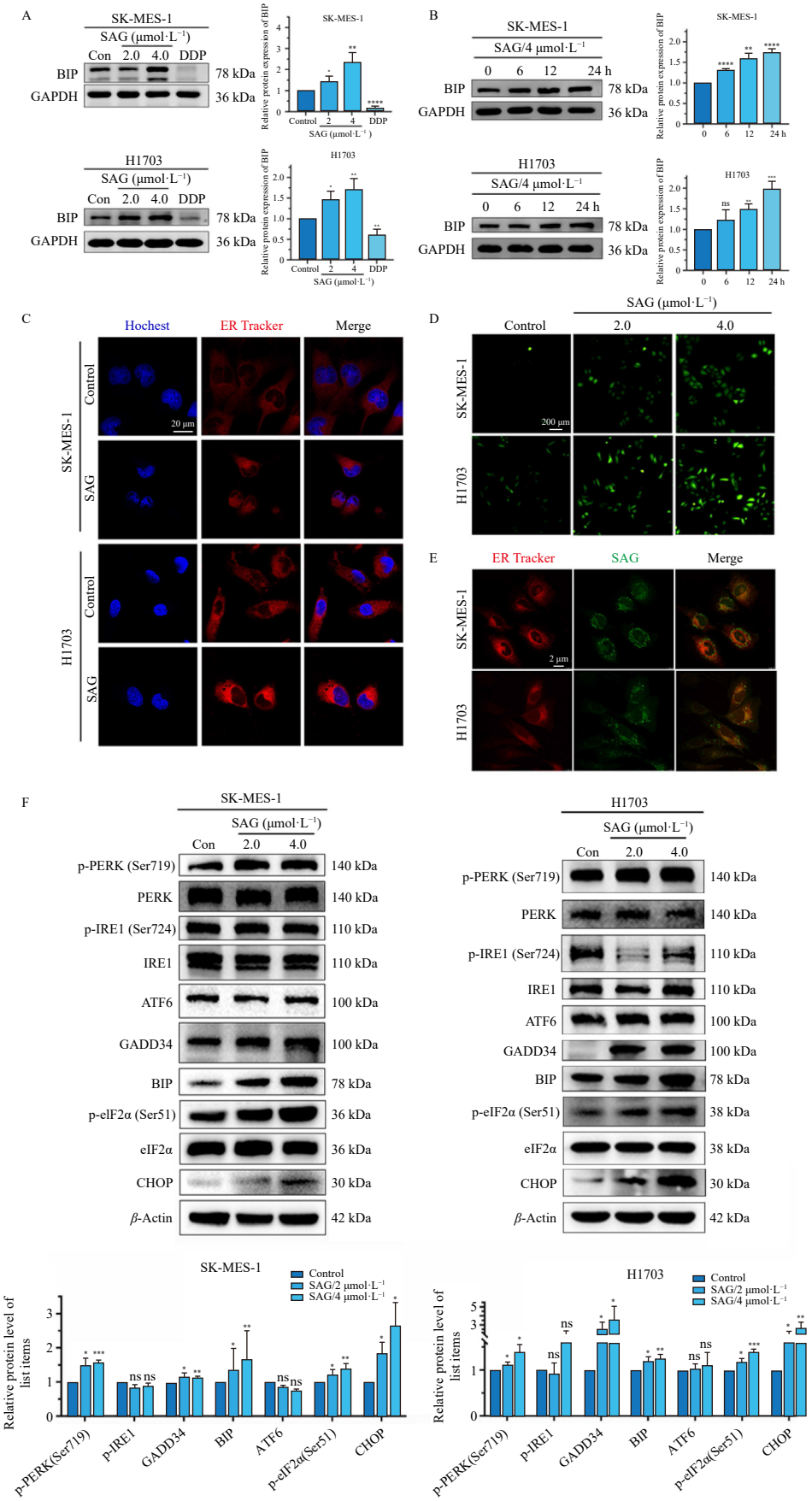

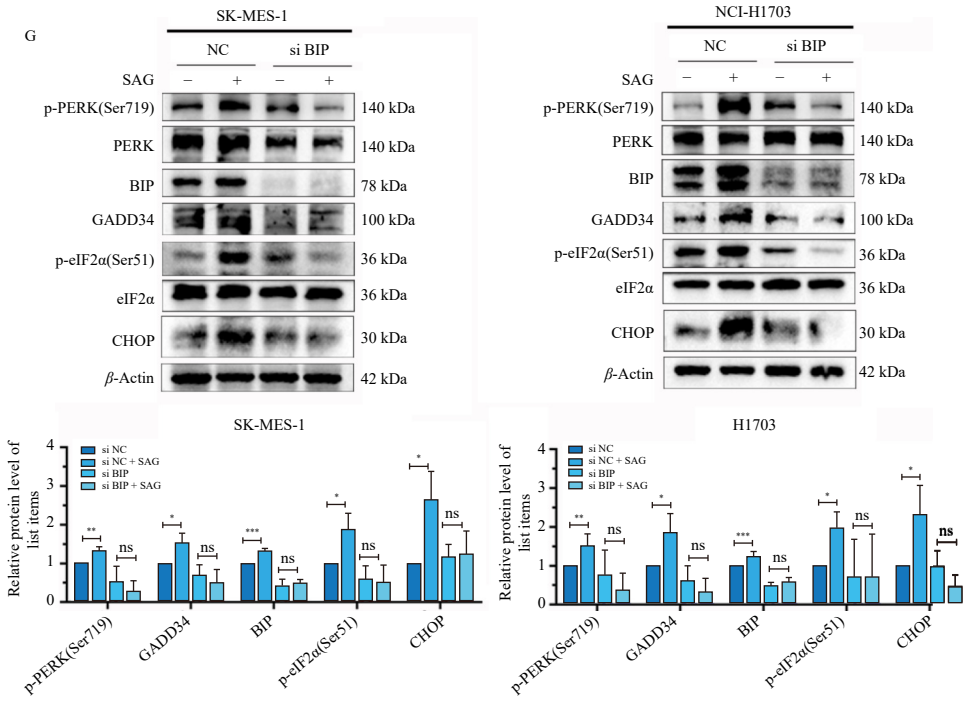

Fig. 6 SAG up-regulates BiP to induce ers. (A–B) WB assay analysis of BiP expression in SK-MES-1 and H1703 cells following SAG treatment in a dose- and time-dependent manner. (C) Morphological changes in the ER of SK-MES-1 and H1703 cells after SAG treatment. Scale bar: 20 μm. (D) Intracellular ROS levels in SK-MES-1 and H1703 cells following SAG treatment. Scale bar: 200 μm(E) Intracellular distribution of SAG in LUSC cells observed by confocal laser microscopy. Scale bar: 2 μm. (F) WB analysis of ER stress-related proteins, including p-PERK (Ser719), PERK, p-IRE1 (Ser724), IRE1, ATF6, GADD34, BiP, p-eIF2α (Ser51), eIF2α, and CHOP, in SK-MES-1 and H1703 cells after SAG treatment. (G) WB analysis of p-PERK (Ser719), PERK, GADD34, p-eIF2α (Ser51), eIF2α, and CHOP in SK-MES-1 and H1703 cells with or without BiP knockdown following SAG treatment. Data are expressed as mean ± SD (n = 3). $^{*}P < 0.05$, $^{**}P < 0.01$, $^{***}P < 0.001$, $^{****}P < 0.0001$; n s., not significant ($P > 0.05$) compared with the 0 μmol·L^{-1} SAG group.

roptosis are functionally interconnected. Ferroptosis is an iron-dependent form of RCD characterized by lipid peroxidation.

Although historically considered distinct, recent studies have demonstrated shared regulatory mechanisms and signaling networks between apoptosis and ferroptosis [31]. Therefore, targeting their crosstalk represents a promising anti-cancer strategy. For example, dihydroartemisinin induces cell death in head and neck cancer by promoting both ferroptosis and apoptosis *via* the modulation of Forkhead box protein M1 (FoxM1) [32]. Moxartenolide, a sesquiterpene lactone from *Artemisia argyi*, inhibits the proliferation of cancer cells by inducing apoptosis and ferroptosis through NDUFA4, an essential enzyme involved in cell metabolism [33]. Agrimonolide suppresses the progression of cancer and triggers both ferroptosis and apoptosis by targeting SCD1 in ovarian cancer cells [34]. Furthermore, ERS has been implicated as a key regulator linking apoptosis and ferroptosis. Activation of ERS-associated signaling molecules, such as XBP1, JNK, and ATF4/CHOP, contributes to the transition between these processes [35]. Consistently, our study demonstrates that SAG induces apoptosis and ferroptosis through direct targeting of BiP, as validated by DARTS, LC-MS/MS, CETSA, and SPR analyses.

BiP, also referred to as GRP78, is a central regulator of ER homeostasis and UPR signaling. It functions both as a molecular chaperone that facilitates protein folding and as a key modulator of UPR activation. Under basal conditions, BiP binds to PERK, IRE1, and ATF6, maintaining these sensors in an inactive state [36]. The UPR comprises two functional phases: an initial adaptive phase that restores ER homeostasis, followed by a pro-death phase when stress is excessive or prolonged [37]. Dysregulation of BiP and sustained UPR activation have been implicated in tumor progression, highlighting BiP as a potential therapeutic target [38]. Various strategies targeting BiP, including antibodies, peptides, and small molecules, have been explored. Natural small molecules, in particular, exhibit favorable properties such as high cell permeability and chemical stability, and can function as either BiP inhibitors or activators [39]. For example, YUM70 binds

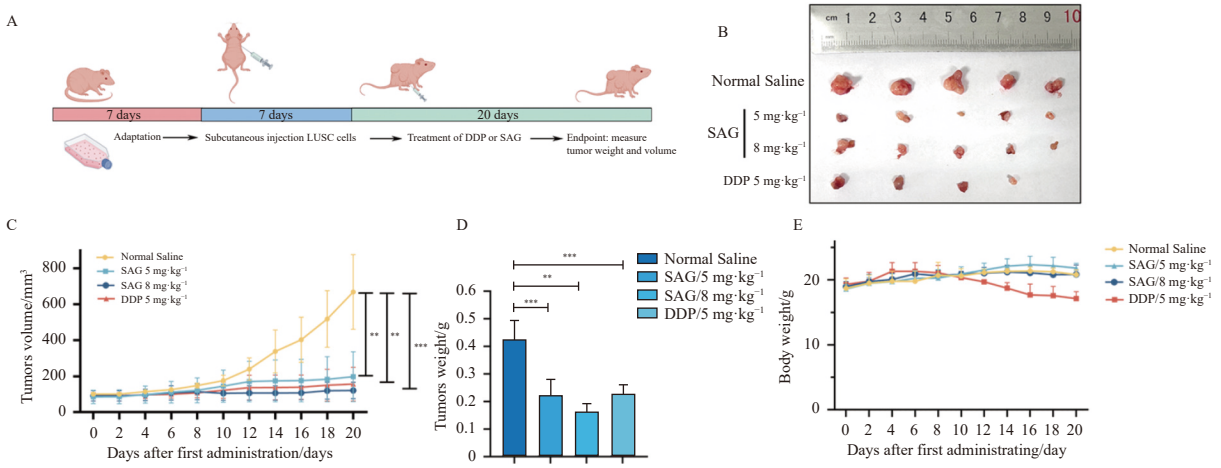

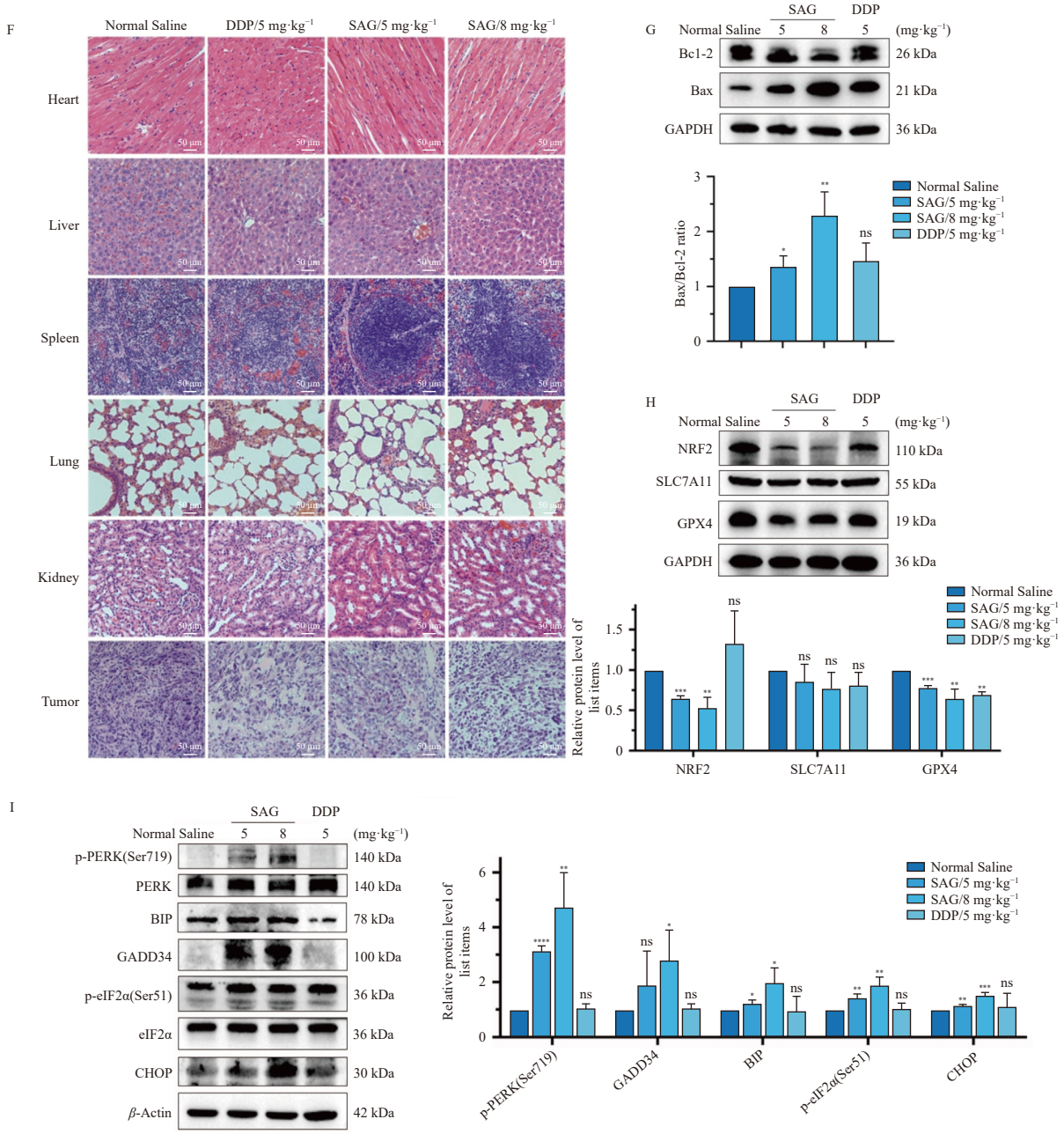

Fig. 7 SAG suppresses tumor growth *in vivo* and is associated with induction of apoptosis and ferroptosis. (A) Schematic illustration of the xenograft nude mouse model and treatment regimen. (B) Representative images of xenograft tumors from different treatment groups (n = 5). (C) Tumor volume curves. (D) Final tumor weights and (E) body weights of xenograft-bearing mice treated with low-dose SAG, high-dose SAG, or DDP for 20 days (n = 6). (F) Representative H&E-stained images of xenograft tumors from different groups. Scale bar: 50 μm (G) WB analysis of Bcl-2 and Bax expression in tumor tissues following SAG or DDP treatment. (H) WB analysis of NRF2, SLC7A11, and GPX4 expression in tumor tissues following SAG or DDP treatment. (I) WB analysis of p-PERK (Ser719), PERK, GADD34, p-eIF2α (Ser51), eIF2α, and CHOP expression in tumor tissues following SAG or DDP treatment. Data are expressed as mean ± SD (n = 3). $^{*}P < 0.05$, $^{**}P < 0.01$, $^{***}P < 0.001$, $^{****}P < 0.0001$; n s., not significant ($P > 0.05$) compared with control group.

directly to BiP, rendering it inactive. This action triggers ERS-mediated apoptosis and enhances the cytotoxic effects of topotecan and vorinostat on pancreatic cancer [14]. Salvianolic acid A reduces the secretion of BiP and facilitates its degradation in the lysosome, ultimately hindering tumour angiogenesis and growth by interacting with BiP [40]. Isoliquiritigenin inhibits the self-renewal, invasion, metastasis, and clone-forming abilities of stem cells in oral squamous cell carcinomas by reducing the expression of the GRP78 mRNA and membrane GRP78 protein [41]. Conversely, certain compounds act as BiP activators. Ginsenoside compound K increases BiP expression, reduces p-STAT3 levels, and triggers ERS and apoptosis in human liver cancer cells [18]. Betulinic acid treatment results in an increase in BiP levels. The elevated BiP levels then trigger the ERS stress sensor PERK, which subsequently phosphorylates eIF2α. This phosphorylation leads to the suppression of β-catenin expression, thereby reducing c-Myc-driven glycolysis [42]. Honokiol markedly diminishes the viability and movement of LUAD cells while promoting cellular apoptosis. This process is accompanied by increased levels of ERS-induced apoptotic signalling molecules, including BiP, phosphorylated PERK, phosphorylated eIF2α, CHOP, Bcl-2, Bax, and cleaved Caspase 9. These findings suggest that triggering ERS-related apoptosis could constitute a new approach for treating human lung cancer [43]. Consistent with these previous studies, we show here that SAG directly binds to BiP and induces BiP expression, triggering ERS in LUSC cells through the phosphorylation of PERK and eIF2α, subsequently upregulating CHOP and leading to ERS-associated apoptosis and ferroptosis.

In summary, our findings reveal a novel mechanism by which SAG targets BiP to induce ERS, thereby activating the PERK/

eIF2α/CHOP/GADD34 signaling cascade and simultaneously triggering apoptosis and ferroptosis in LUSC cells. However, several limitations should be noted, including the lack of precise characterization of the SAG-binding site on BiP and the limited evaluation of SAG pharmacokinetics and bioavailability. Despite these limitations, our findings provide new mechanistic insights and support the potential of SAG as a therapeutic agent for LUSC and potentially other squamous cell carcinomas.

5. Conclusions

In conclusion, this study is the first to demonstrate that SAG exerts anti-tumor activity against LUSC by concurrently inducing apoptosis and ferroptosis through direct targeting of BiP and activation of the PERK/eIF2α/CHOP/GADD34 pathway. These findings provide critical insights into the potential clinical application of SAG in LUSC treatment (Fig. 8).

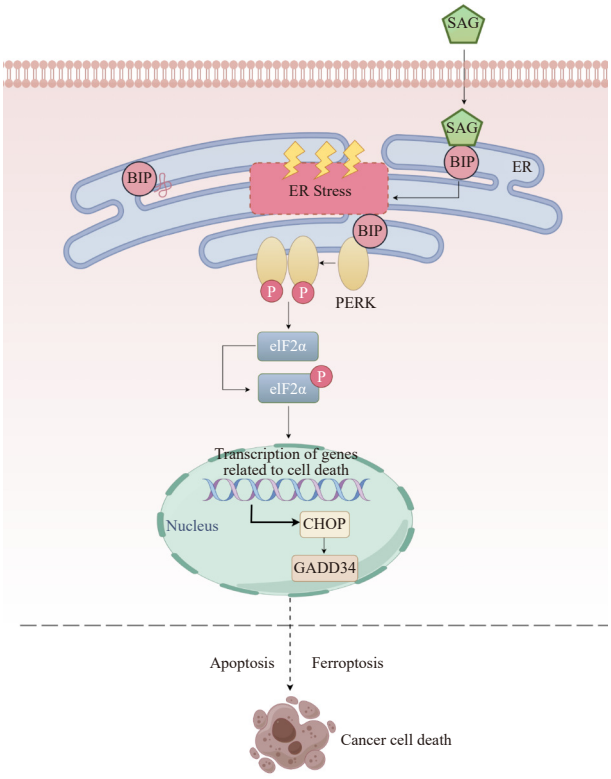

Fig. 8 Schematic diagram of the mechanism of SAG-induced apoptosis and ferroptosis in LUSC cells.

Funding

This work was supported by the National Natural Science Foundation of China (Nos. U25A20166, 82374093 and 82460718), the Joint Project on Regional High-Incidence Diseases Research of Guangxi Natural Science Foundation (No. 2023GXNSFDA026026), and the Natural Science Foundation of Guangxi Province (No. 2023GXNSFAA026224).

Declaration of competing interest

These authors declare no conflict of interest.

Acknowledgement

We express our gratitude to the research team of Prof. Huaxin Hou and Prof. Danrong Li, along with Dr. Li Li, who provided countless help and patience during experiment process.

References

1 Sung H, Ferlay J, Siegel RL, et al. Global Cancer Statistics 2020: GLOBOCAN estimates of incidence and mortality worldwide for 36 cancers in 185 countries. *CA Cancer J Clin*. 2021;71(3):209-249. https://doi.org/10.3322/caac.21660.
2 Lau SCM, Pan YW, Velcheti V, et al. Squamous cell lung cancer: current landscape and future therapeutic options. *Cancer Cell*. 2022;40(11):1279-1293. https://doi.org/10.1016/j.ccell.2022.09.018.
3 Pan YW, Han H, Labbe KE, et al. Recent advances in preclinical models for lung squamous cell carcinoma. *Oncogene*. 2021;40(16):2817-2829. https://doi.org/10.1038/s41388-021-01723-7.
4 Chen MJ, Ma PF, Zhang YC, et al. Divergent tumor and immune cell reprogramming underlying immunotherapy response and immune-related adverse events in lung squamous cell carcinoma. *J Immunother Cancer*. 2023;11(10):e007305. https://doi.org/10.1136/jitc-2023-007305.
5 Gandara DR, Hammerman PS, Sos ML, et al. Squamous cell lung cancer: from tumor genomics to cancer therapeutics. *Clin Cancer Res*. 2015;21(10):2236-2243. https://doi.org/10.1158/1078-0432.CCR-14-3039.
6 Tabas I, Ron D. Integrating the mechanisms of apoptosis induced by endoplasmic reticulum stress. *Nat Cell Biol*. 2011;13(3):184-190. https://doi.org/10.1038/ncb0311-184.
7 He F, Zhang P, Liu JL, et al. ATF4 suppresses hepatocarcinogenesis by inducing SLC7A11 (xCT) to block stress-related ferroptosis. *J Hepatol*. 2023;79(2):362-377. https://doi.org/10.1016/j.jhep.2023.03.016.
8 Schleicher SM, Moretti L, Varki V, et al. Progress in the unraveling of the endoplasmic reticulum stress/autophagy pathway and cancer: implications for future therapeutic approaches. *Drug Resist Updat*. 2010;13(3):79-86. https://doi.org/10.1016/j.drup.2010.04.002.
9 Li HL, Deng XY, Zhang ZW, et al. Nitric oxide/paclitaxel micelles enhance anti-liver cancer effects and paclitaxel sensitivity by inducing ferroptosis, endoplasmic reticulum stress and pyroptosis. *RSC Adv*. 2023;13(45):31772-31784. https://doi.org/10.1039/D3RA04861F.
10 Hetz C, Zhang K, Kaufman RJ. Mechanisms, regulation and functions of the unfolded protein response. *Nat Rev Mol Cell Biol*. 2020;21(8):421-438. https://doi.org/10.1038/s41580-020-0250-z.
11 Iurlaro R, Muñoz-Pinedo C. Cell death induced by endoplasmic reticulum stress. *FEBS J*. 2016;283(14):2640-2652. https://doi.org/10.1111/febs.13598.
12 Banach A, Jiang YP, Roth E, et al. CEMIP upregulates BiP to promote breast cancer cell survival in hypoxia. *Oncotarget*. 2019;10(42):4307-4320. https://doi.org/10.18632/oncotarget.27036.
13 Roué G, Pérez-Galán P, Mozos A, et al. The Hsp90 inhibitor IPI-504 overcomes bortezomib resistance in mantle cell lymphoma *in vitro* and *in vivo* by down-regulation of the prosurvival ER chaperone BiP/Grp78. *Blood*. 2011;117(4):1270-1279. https://doi.org/10.1182/blood-2010-04-278853.
14 Samanta S, Yang SH, Debnath B, et al. The hydroxyquinoline analogue YUM70 inhibits GRP78 to induce ER stress-mediated apoptosis in pancreatic cancer. *Cancer Res*. 2021;81(7):1883-1895. https://doi.org/10.1158/0008-5472.CAN-20-1540.
15 Ma FF, Ma RH, Thakur K, et al. miRNA omics reveal neferine induces apoptosis through Ca^{2+} mediated endoplasmic reticulum stress pathway in human endometrial cancer. *Phytomedicine*. 2024;134:155988. https://doi.org/10.1016/j.phymed.2024.155988.
16 Jiang DD, Guo YM, Wang TY, et al. IRE1α determines ferroptosis sensitivity through regulation of glutathione synthesis. *Nat Commun*. 2024;15(1):4114. https://doi.org/10.1038/s41467-024-48330-0.
17 Cao W, Liu TT, Yang ST, et al. Efficient synthesis of icetexane diterpenes and apoptosis inducing effect by upregulating BiP-ATF4-CHOP axis in colorectal cells. *J Nat Prod*. 2021;84(7):2012-2019. https://doi.org/10.1021/acs.jnatprod.1c00310.
18 Zhang X, Zhang SL, Sun QT, et al. Compound K induces endoplasmic reticulum stress and apoptosis in human liver cancer cells by regulating STAT3. *Molecules*. 2018;23(6):1482. https://doi.org/10.3390/molecules23061482.
19 Luo FH, Chen ZH, Zeng FF, et al. Botany, phytochemistry, pharmacologic activities, traditional applications, pharmacokinetics, quality control and toxicity of Zanthoxyli Radix: an updated review. *J Ethnopharmacol*. 2025;337(Pt 1):118783. https://doi.org/10.1016/j.jep.2024.118783.
20 Fan HN, Chen W, Peng SQ, et al. Sanguinarine inhibits the tumorigenesis of gastric cancer by regulating the TOX/DNA-PKcs/ KU70/80 pathway. *Pathol Res Pract*. 2019;215(11):152677. https://doi.org/10.1016/j.prp.2019.152677.
21 Qi XY, Chen YL, Liu S, et al. Sanguinarine inhibits melanoma invasion and migration by targeting the FAK/PI3K/AKT/mTOR signalling pathway. *Pharm Biol*. 2023;61(1):696-709. https://doi.org/10.1080/13880209.2023.2200787.
22 Xu RZ, Wu JC, Luo YB, et al. Sanguinarine represses the growth and metastasis of non-small cell lung cancer by facilitating ferroptosis. *Curr Pharm Des*. 2022;28(9):760-768. https://doi.org/10.2174/1381612828666220217124542.
23 Direito I, Gomes D, Monteiro FL, et al. The clinicopathological significance of BiP/GRP-78 in breast cancer: a meta-analysis of public datasets and immunohistochemical detection. *Curr Oncol*. 2022;29(12):9066-9087. https://doi.org/10.3390/curroncol29120710.
24 Achkar IW, Mraiche F, Mohammad RM, et al. Anticancer potential of sanguinarine for various human malignancies. *Future Med Chem*. 2017;9(9):933-950. https://doi.org/10.4155/fmc-2017-0041.
25 Fu CX, Guan GP, Wang HB. The anticancer effect of sanguinarine: a review. *Curr Pharm Des*. 2018;24(24):2760-2764. https://doi.org/10.2174/1381612824666180829100601.

26 Choi YH, Choi WY, Hong SH, et al. Anti-invasive activity of sanguinarine through modulation of tight junctions and matrix metalloproteinase activities in MDA-MB-231 human breast carcinoma cells. *Chem Biol Interact*. 2009;179(2-3):185-191. https://doi.org/10.1016/j.cbi.2008.11.009.

27 Qin TT, Li ZH, Li LX, et al. Sanguinarine, identified as a natural alkaloid LSD1 inhibitor, suppresses lung cancer cell growth and migration. *Iran J Basic Med Sci*. 2022;25(6):781-788. https://doi.org/10.22038/IJBMS.2022.62541.13851.

28 Prabhu KS, Bhat AA, Siveen KS, et al. Sanguinarine mediated apoptosis in non-small cell lung cancer *via* generation of reactive oxygen species and suppression of JAK/STAT pathway. *Biomed Pharmacother*. 2021;144:112358. https://doi.org/10.1016/j.biopha.2021.112358.

29 Hanahan D. Hallmarks of cancer: new dimensions. *Cancer Discov*. 2022;12(1):31-46. https://doi.org/10.1158/2159-8290.CD-21-1059.

30 Peng F, Liao MR, Qin R, et al. Regulated cell death (RCD) in cancer: key pathways and targeted therapies. *Signal Transduct Target Ther*. 2022;7(1):286. https://doi.org/10.1038/s41392-022-01110-y.

31 Wu PY, Zhang XY, Duan DY, et al. Organelle-specific mechanisms in crosstalk between apoptosis and ferroptosis. *Oxid Med Cell Longev*. 2023;2023:3400147. https://doi.org/10.1155/2023/3400147.

32 Lin RY, Zhang ZH, Chen LF, et al. Dihydroartemisinin (DHA) induces ferroptosis and causes cell cycle arrest in head and neck carcinoma cells. *Cancer Lett*. 2016;381(1):165-175. https://doi.org/10.1016/j.canlet.2016.07.033.

33 Wang ZL, Li ZY, Ji RS, et al. Sesquiterpene lactone from *Artemisia argyi* inhibited cancer proliferation by inducing apoptosis and ferroptosis *via* key cell metabolism enzyme NDUFA4. *Phytomedicine*. 2025;136:156312. https://doi.org/10.1016/j.phymed.2024.156312.

34 Liu Y, Liu XB, Wang H, et al. Agrimonolide inhibits cancer progression and induces ferroptosis and apoptosis by targeting SCD1 in ovarian cancer cells. *Phytomedicine*. 2022;101:154102. https://doi.org/10.1016/j.phymed.2022.154102.

35 Vinik Y, Maimon A, Dubey V, et al. Programming a ferroptosis-to-apoptosis transition landscape revealed ferroptosis biomarkers and repressors for cancer therapy. *Adv Sci (Weinh)*. 2024;11(17):e2307263. https://doi.org/10.1002/advs.202307263.

36 Kopp MC, Larburu N, Durairaj V, et al. UPR proteins IRE1 and PERK switch BiP from chaperone to ER stress sensor. *Nat Struct Mol Biol*. 2019;26(11):1053-1062. https://doi.org/10.1038/s41594-019-0324-9.

37 Roller C, Maddalo D. The molecular chaperone GRP78/BiP in the development of chemoresistance: mechanism and possible treatment. *Front Pharmacol*. 2013;4:10. https://doi.org/10.3389/fphar.2013.00010.

38 Akinyemi AO, Simpson KE, Oyelere SF, et al. Unveiling the dark side of glucose-regulated protein 78 (GRP78) in cancers and other human pathology: a systematic review. *Mol Med*. 2023;29(1):112. https://doi.org/10.1186/s10020-023-00706-6.

39 Guo WK, Wang MJ, Yang ZF, et al. Recent advances in small molecule and peptide inhibitors of glucose-regulated protein 78 for cancer therapy. *Eur J Med Chem*. 2023;261:115792. https://doi.org/10.1016/j.ejmech.2023.115792.

40 Yang YF, Zhang LC, La XQ, et al. Salvianolic acid A inhibits tumor-associated angiogenesis by blocking GRP78 secretion. *Naunyn Schmiedebergs Arch Pharmacol*. 2019;392(4):467-480. https://doi.org/10.1007/s00210-018-1585-2.

41 Hu FW, Yu CC, Hsieh PL, et al. Targeting oral cancer stemness and chemoresistance by isoliquiritigenin-mediated GRP78 regulation. *Oncotarget*. 2017;8(55):93912-93923. https://doi.org/10.18632/oncotarget.21338.

42 Zheng YF, Liu PX, Wang N, et al. Betulinic acid suppresses breast cancer metastasis by targeting GRP78-mediated glycolysis and ER stress apoptotic pathway. *Oxid Med Cell Longev*. 2019;2019:8781690. https://doi.org/10.1155/2019/8781690.

43 Zhu JF, Xu SN, Gao WL, et al. Honokiol induces endoplasmic reticulum stress-mediated apoptosis in human lung cancer cells. *Life Sci*. 2019;221:204-211. https://doi.org/10.1016/j.lfs.2019.01.046.